Naval Research Laboratory
Washington, DC 20375-5320

NRL/MR/6003--19-9843

Health-Effect Hazard Areas for Airborne Contaminant Agents

Jay Boris
Gopal Patnaik
Keith Obenschain

Laboratories for Computational Physics and Fluid Dynamics Branch
Material Science & Component Technology Directorate

January 15, 2019

REPORT DOCUMENTATION PAGE

Form Approved
OMB No. 0704-0188

1. REPORT DATE *(DD-MM-YYYY)*
15-01-2019

2. REPORT TYPE
Memorandum Report

3. DATES COVERED *(From - To)*

4. TITLE AND SUBTITLE
Health-Effect Hazard Areas for Airborne Contaminant Agents

5a. CONTRACT NUMBER

5b. GRANT NUMBER
64-1G56-0-9-5

5c. PROGRAM ELEMENT NUMBER

6. AUTHOR(S)
Jay Boris, Gopal Patnaik and Keith Obenschain

5d. PROJECT NUMBER

5e. TASK NUMBER

5f. WORK UNIT NUMBER

7. PERFORMING ORGANIZATION NAME(S) AND ADDRESS(ES)
U.S. Naval Research Laboratory
4555 Overlook Avenue, SW
Washington, DC 20375-5320

8. PERFORMING ORGANIZATION REPORT NUMBER
NRL/MR/6003--19-9843

9. SPONSORING / MONITORING AGENCY NAME(S) AND ADDRESS(ES)

10. SPONSOR / MONITOR'S ACRONYM(S)

11. SPONSOR / MONITOR'S REPORT NUMBER(S)

12. DISTRIBUTION / AVAILABILITY STATEMENT
DISTRIBUTION STATEMENT A: Approved for public release; distribution is unlimited.

13. SUPPLEMENTARY NOTES

14. ABSTRACT

Because inhalation toxicity of an airborne contaminant usually depends nonlinearly on the agent density, time-dependent, naturally-occurring density fluctuations in open-air release scenarios have a disproportionately large effect on the time symptoms will onset. A wide range of integrated toxic loads is found for different realizations of the same release and thus the onset of health-effect symptoms occurs over a wide range of exposure durations. This naturally occurring variability makes integrating a model of a representative or average agent density time history of relatively little value to determine the toxicity one can expect. Rather, the statistical distribution of possible toxic load integrals must be taken into account and this is heavily dependent on low-probability realizations that are difficult to obtain in field trials, wind tunnel experiments, and simulations. What real-time users of a predictive model need to know is whether the symptoms of whatever adverse health-effect being considered can occur with unacceptably high probability and what is the earliest possible time this symptom onset can occur.

This paper reports a major simplification in computing these toxic agent health effects that accounts for the presence of large fluctuations and the corresponding low-probability scenarios that result from these fluctuations. This new approach requires minimal agent time history data and so identifies the most dangerous, plausible "worst-case" health-effects for urban scenarios. We will present the distributions of possible toxic load integrals in terms of two time independent quantities, the ensemble maximum density and earliest agent arrival time at each location and we will show how this information gives a simple, fast method to compute the earliest (i.e. most conservative) symptom onset time for real-time contaminant transport software systems such as NRL's CT-Analyst®.

15. SUBJECT TERMS
Airborne contaminant agents
Wind tunnel experiments
Toxic agent health effects
Time-dependent

16. SECURITY CLASSIFICATION OF:			17. LIMITATION OF ABSTRACT	18. NUMBER OF PAGES	19a. NAME OF RESPONSIBLE PERSON
a. REPORT	**b. ABSTRACT**	**c. THIS PAGE**			Jay Boris
Unclassified Unlimited	Unclassified Unlimited	Unclassified Unlimited	Unclassified Unlimited	23	**19b. TELEPHONE NUMBER** *(include area code)* 202-767-3055

Standard Form 298 (Rev. 8-98)
Prescribed by ANSI Std. Z39.18

This page intentionally left blank.

I. Introduction and Background

This paper considers the computation of health-effect hazard areas resulting from localized, short-duration "puff" releases of airborne toxic contaminants (agents). The natural variability of the wind in a complex-geometry region such as a city leads to wide fluctuations in the airborne agent densities, in their time histories, and in their accumulated doses at any location in the domain. Surprisingly, computing a plausible worst-case health-effect hazard area, which is what people need to know, will be shown to become tractably simple by considering only the earliest likely onset time for a particular health effect (i.e. "symptom"). This paper reports a major simplification in computing these toxic agent health effects that accounts for the presence of large fluctuations due to natural wind variability exacerbated by the complex geometry. This new approach requires minimal agent time history data and also reduces uncertainty in the worst-case health-effect predictions. We will show distributions of possible toxic load integrals in terms of two time-independent quantities, the maximum agent density and the earliest agent arrival time at each location in the domain and how this information gives a simple, fast way to compute the time of earliest symptom onset at each point.

Since inhalation toxicity usually depends nonlinearly on the contaminating agent density, time-dependent, naturally occurring density fluctuations in open-air release scenarios have a disproportionately large effect on the overall symptom onset time. A very wide range of toxic load integrals is found for different realizations of the same release even when the toxic loading is linear and depends only on the dose. This natural variability makes integrating a model of a representative agent density time history of relatively little value. Rather, the statistical distribution of possible toxic load integrals for the ensemble of possible realizations of a release event in a given environmental condition must be taken into account. Atmospheric transport and dispersion models provide estimations of a plume's movement and the associated agent density variations in 2D and 3D, but most crisis managers would like to see these results expressed in terms of the likely health effects – and get the information while there is still time to respond to and hopefully mitigate the threat. What these users need to know is whether symptoms, at whatever health-effect level is being considered, can occur with unacceptably high probability and what is the earliest possible time these symptoms can onset.

The toxic load calculations discussed in this paper are based on the three EPA Acute Exposure Guideline Levels (AEGL 1, AEGL 2, and AEGL 3) for predicting the onset of adverse health effects for a general population that inhales specific duration exposures to specific concentrations of toxic chemicals. The material on the AEGLs is openly available on the internet (https://www.epa.gov/aegl, 2018). A number of organizations, agencies and nations use these guidelines and may even mandate this approach to standardize estimating and reporting toxic health effects. The main drawback of the AEGLs is that only a few fixed-duration exposures to a few constant-density conditions are tabulated. The issue of how to treat real toxic plumes, whose agent density varies strongly and often quickly in space and time, is left undefined.

In an earlier report, Boris and Patnaik (2014), developed a new algorithm to integrate toxic loads accurately based on a nonlinear, density-dependent model derived from, and fully consistent with, the data in the AEGL tables. This algorithm and software package, called EAGLE, computes the onset of AEGL 1 (notable discomfort), AEGL 2 (irreversible or serious adverse impact), and AEGL 3 (life threatening or death) health-effects (symptoms) in response to general,

____

Manuscript approved January 15, 2019.

time-varying concentration profiles that usually don't satisfy the specific constant-density-over-an-extended-period conditions expressed by EPA in the tabulated AEGLs. The AEGL 1, 2, or 3 onset conditions for any agent concentration history can be computed without reference to any particular pre-tabulated concentration or exposure duration. Plumes over entire urban areas can be integrated in a few seconds, making EAGLE well suited to use with a dispersion model or CFD code. Eagle, in and of itself, however, is not the answer to calculating the onset of health effects.

The EAGLE algorithm is based on an application of the 'Induction Parameter Model' developed in 1980 for fast combustion and explained in detail in the book "Numerical Simulation of Reactive Flow", (Oran and Boris, 2001, 2nd edition). The present application to potentially toxic plumes uses the ten Berge generalization of Haber's law (e.g. ten Berge, *et al.,* 1986; Stage, 2004; Sweeney, *et al.,* 2014) integrated against a given agent density time history. The new calculation is simple, very fast, and can be applied to any chemical or agent for which the AEGL onset conditions have been tabulated by EPA.

Figure 1. Continuous (steady) sources and acute (instantaneous) sources lay down a gaseous tracer at the 6 locations indicated above in a 6 km by 4 km urban domain. The wind is from 300^0 at 3.0 m/s and the temperature is 0^{0}C. The cell size for the FAST3D-CT simulation was 5 meters.

A database of time-dependent density profiles of acute puff and continuous plume releases in a fictitious urban domain has been constructed for studies like this. The draft report is entitled "Airborne Puff and Plume Datasets for an Urban Landscape" (Boris and Obenschain, 2018). Figure 1 above shows the urban geometry of this database, a 6 km by 4 km urban region where the building outlines are contoured at ground level. NRL's FAST3D-CT MILES simulation model (Patnaik and Boris, 2005; Patnaik, *et al*, 2007; Boris, *et al.,* 2009, 2010) was run for this 3D geometry at 5-meter spatial resolution with a 3 m/s wind from 300^0 (30^0 north of west). The average velocity and temperature profiles were provided by NRL's COAMPS-OS model (Holt, *et* *al.,* 2009, 2011) and natural fluctuations at the domain boundaries were imposed on the average profiles using a formulation that has been developed for FAST3D-CT and validated through the OKC field trials and in the University of Hamburg wind tunnel.

After a CFD spin-up interval of 15,000 steps had elapsed (25 minutes), each of the six sources in Fig. 1 above was switched on and continuously emitted thereafter throughout the duration of the run, almost 8 hours real time. The six agent plume densities were recorded every 25 timesteps (2.5 seconds) at ground level across the entire domain for 300,000 timesteps (including the initial spin-up). The resulting plume data set allows a number of analyses to be performed. The main applications of this plume component of the database have been in the extent, distribution, and time spectrum of the density fluctuations and in the intermittency of the flow as reflected in the time-varying agent density.

The second half of the database records the time histories of instantaneous (acute) agent releases, often called puffs, from each of the source locations in Fig. 1. 16 separate realizations of a puff at each of the 6 source locations was run for 100 minutes of real time. Ground-level cross sections from each of these 96 puff releases were recorded every 10 seconds for 100 minutes of real time. The main applications of this puff component of the database have been seeking approximations for acute-source density distribution functions, studying the effects of geometry on the density time histories, and studies of agent toxicity effects leading to this paper.

II. The Effect of Nonlinearity on the Integrated Toxic Load of an Agent

The first use of the EAGLE package and the plume database described here, furthering the background discussion, is a comparison of the toxic load from the actual time-dependent plume from one of the sources integrated over two hours, with the same integrated toxic load using the average plume density over the same two-hour period. The plume density is low enough in this example that buoyancy effects are not important and we are treating the agent as chlorine in this particular comparison. Chlorine, over much of the density range has a quadratic toxicity. Figure 2 shows where the toxic load integral exceeds unity, in other words the hazard area, for AEGL 1, 2, and 3, at each of the cells in the domain.

On the left in Fig. 2 we show an instantaneous color contour plot of the ground-level chlorine density computed by FAST3D-CT and taken two hours after the continuous source S4 begins emitting in the upper left of the domain (northwest). This source location is marked with the yellow circle at the upper left end of the lavender high-density region, which is just to the right of the label "Source 4". The building cross sections at ground level appear white in the figures assuming that no chlorine penetrates the buildings. FAST3D-CT is a time-dependent Monotone Integrated Large Eddy Simulation (MILES) model with a the relevant complex-geometry physics including solar heating with shadows. It has been validated extensively with wind tunnel data and field trials in Los Angeles, Oklahoma City, New York City and Hamburg Germany.

Every 2.5 seconds the computed ground-level density from FAST3D-CT was saved and summed to compute the running density average, shown at 2 hours on the right in Fig. 2. These time-averaged densities are smoother than the instantaneous snapshot on the left and appear to extend beyond the bounds of the instantaneous plume in some locations. This correct running average approximates what Reynolds-Averaged Navier-Stokes (RANS) or other steady-state/time-averaging/ensemble models might predict the density to be. The density differences between instantaneous and time-averaged densities do not appear to be great when viewed with a logarithmic color map as in Fig. 4, but their effect on the AEGL regions computed is the two density approximations is important.

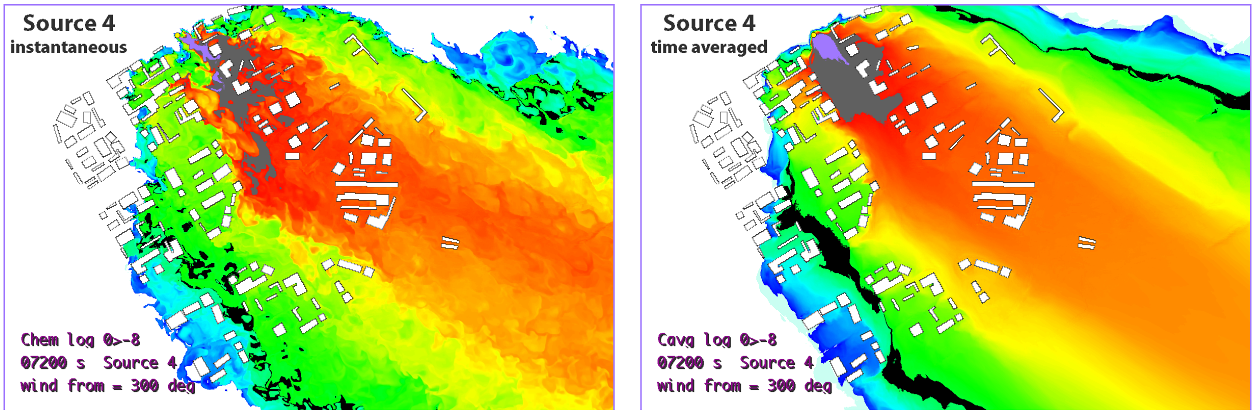

Figure 2. Instantaneous plume (left) and time averaged plume (right) for the continuous release of chlorine from Source 4 located in the upper left of the 6 km by 4 km domain. Density is shown on a logarithmic scale with black bands indicating concentration values near 0.05 ppm.

Figure 3 below compares the AEGL exposure hazard area predictions, based on the FAST3D-CT time-varying plume, using the time-dependent AEGL integration routine in EAGLE. The two panels below show the AEGL 1 (yellow), AEGL 2 (red), and AEGL 3 (black) hazard areas with and without the natural density fluctuations, arising from the fluctuating and gusting 3D winds through the urban geometry. The figure also lists the predicted hazard areas in square kilometers for the two contrasting cases. The area ratios are written on the right-hand panel for comparison. In this example, the hazard areas associated with AEGL 1, 2, and 3 are two to three times larger when realistic fluctuations are taken into account.

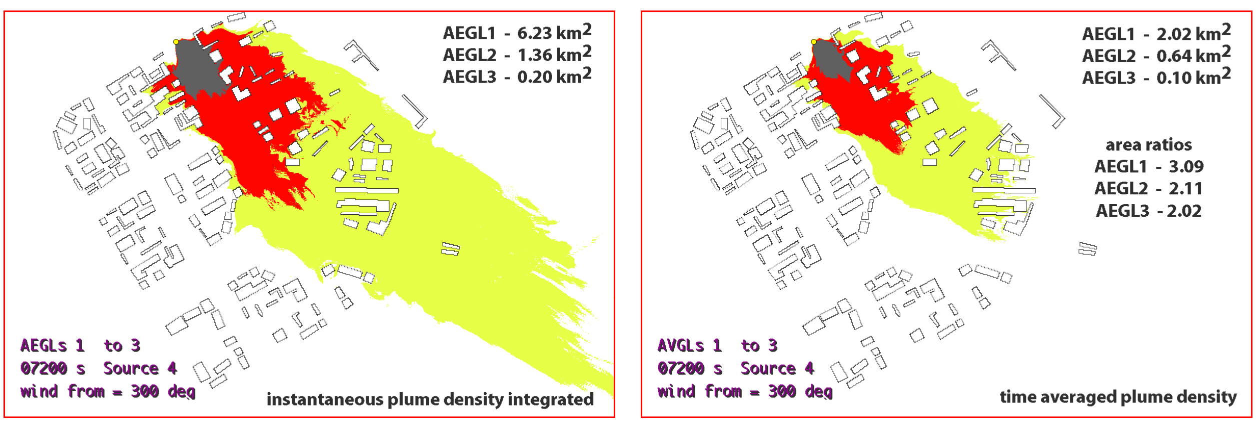

Figure 3. AEGL 1 (yellow), AEGL 2 (red), and AEGL 3 (gray) exposure hazard areas at 2 hours after release computed using the new generalized AEGL routines to integrate the actual, ground level, time-varying densities (left) and the corresponding time-averaged density profiles (right). Natural fluctuations in the density (left), interacting with the non-linear toxic-load behavior of the EPA AEGL tables, increase the hazard areas appreciably.

Including realistic agent density fluctuations increases the hazard area even when the other conditions are all the same. This is not unexpected since it has been recognized for some time that toxic load accumulates much faster than linearly in higher-density regions for many agents.

This is further corroborated in Fig. 3 by the fact that the AEGL 1 hazard area ratio, which is based on a limiting threshold of 0.5 ppm, is larger than the AEGL 2 and AEGL 3 ratios that result from a nearly quadratic dependence of accumulation rate with concentration. Figures 2 and 3 are based on continuous release of agent at the Source 4 location shown. Source 4 was chosen above because the plume extends diagonally across most of the domain, giving the largest contaminated area and the largest possible distances from the source inside the computaional domain. AEGL 1, for the time-dependent plume is entirely in the domain.

With this background, we next consider instantaneous sources, often called acute or puff sources. As one can imagine, a continuous source allows appreciable averaging as the wind gusts and fluctuations wash back and forth across the geometry downwind of the source location. Visually the left and right panels of Fig. 2 appear quite similar. Puff sources, however, further accentuate the effects of these naturally-occurring fluctuations.

III. Puff Releases in an Urban Landscape

Figure 4, immediately below, shows two areas of potential density measurement locations downwind of Sources 3 and 4. These 1 km by 1 km square areas are the locations of various toxic load integrations using the EAGLE package. We seek a simple, useable approximation to density complex traces and their implied toxic loads. Sources 3 and 4 were chosen because they have the longest footprints in the domain with both open areas and areas cluttered with buildings.

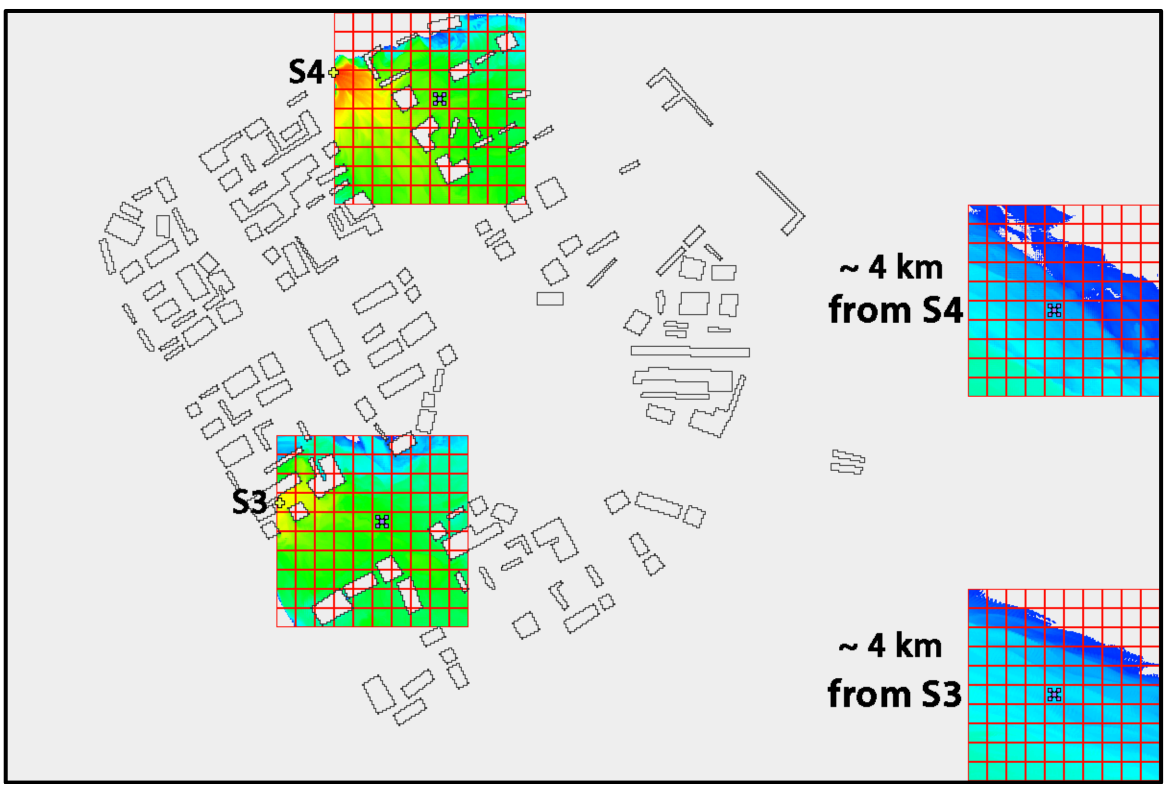

Figure 4: Four distinct 1 km^2 patches in the Source 3 and Source 4 hazard areas display portions of an agent puff. The two patches on the left include the source locations (yellow crosses) for S3 and S4. The 1 km^2 patches for S3 and S4 contain small lavender Xs marking the measurement locations of the density time histories, some of which are shown in Figs. 5 and 6 and in Table 1.

For each source, two km^2 areas are shown illusrating typical agent puff densities. Two of these areas are immediately adjacent to S3 and S4 to capture close in building effects and two are situated on the domain outflow boundary in open areas away from buildings. The lavender X near the center of each 1 km^2 measurement area marks 5 cells for detailed consideration.

Figure 5 depicts the time-history traces of density from the 16 independent instantaneous puff releases at the Source 3 location shown in Fig. 4 above. These time histories are recorded at the center of the lavender X located about 570 m downwind of S3. Each of the 16 independent realizations is plotted in a different color. The fluctuations in density are so severe that nearly all realizations record zero density at the measurement location a number of times. The lavender-on-black curve in the foreground is a smooth analytic approximation to the average of the 16 realizations. Even if this approximation were easily available in operational crisis-management software, however, integrating the toxic load using EAGLE would be inaccurate because all traces have finite periods where they exceed the average by a factor of ten or more. The toxic loading rate will be a factor of 100 or more faster than the average in these periods.

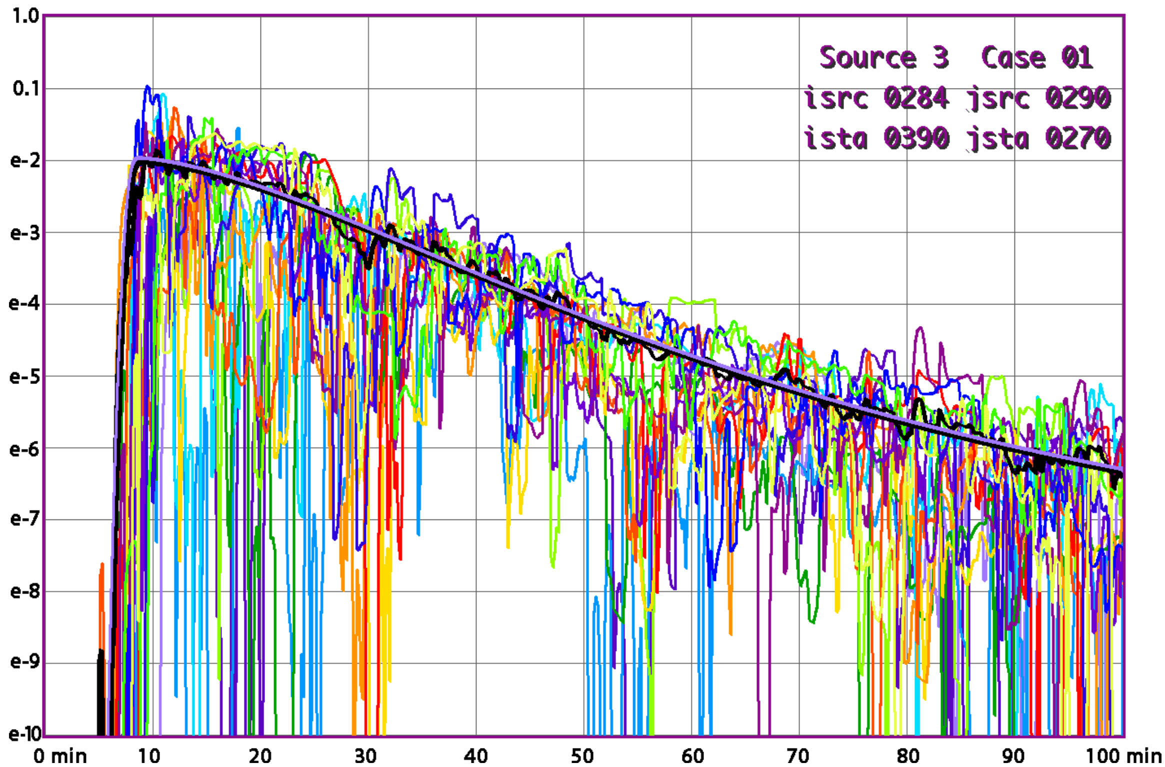

Figure 5: Agent density (gm/m^3) vs time (min) for 16 independent realizations (16 colors) of a short duration "puff" released at S3 and measured about 570 m downwind. An analytic fit to the average of these 16 density traces is drawn as the lavender-on-black curve.

Figure 6 is computed as Fig. 5 but the measurement location is now at the lavender X in the middle of the Source 3 square kilometer in the lower right corner of Fig. 4 below. The I and j cell indices for the source location and the measure station location are given in the upper right corner of Figs. 5 and 6. The agent takes about 20 minutes longer to reach the downwind locations in Fig. 6 than in Fig. 5, which are about 3.5 km farther upwind. Also, the peak densities in Fig. 6 are about two or three orders of magnitude lower than in Fig. 5.

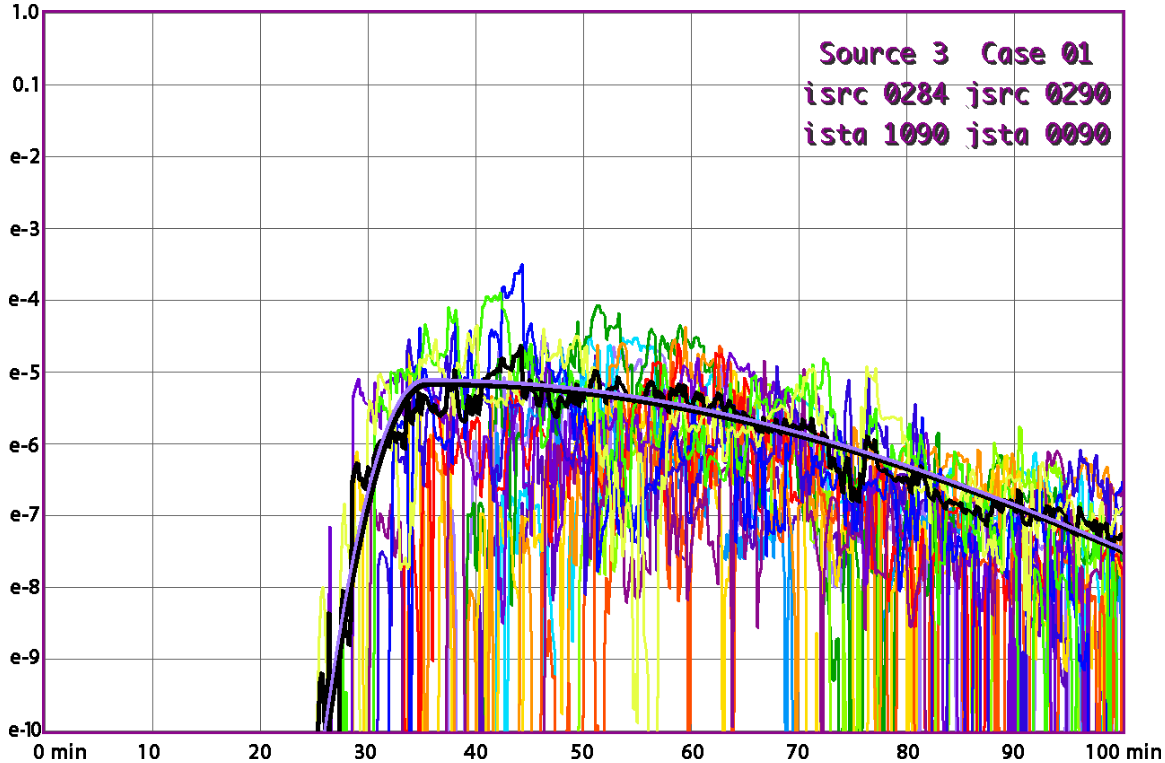

Figure 6: Agent density (gm/m^3) vs time (min) for 16 independent realizations (16 colors) of a short duration "puff" released at S3 and measured about 4 km downwind of the source. An analytic fit to the average of these 16 density traces is drawn as the lavender-on-black curve.

A logarithmic density scale on the left is used in these two figures, emphasizing the decaying nature of the density values in time. This decay, however, is not quite exponential; it slows down as the density drops later in time. This behavior is typical of urban scenarios with an acute puff source. Agent gets trapped in many different places in an urban geometry and is slowly released as a result of vortex shedding behind buildings. Since each of these trapping areas has a different clear-out rate, a larger fraction of the remaining agent, later in time, is still trapped in areas where the clear-out rate is slower.

Depending on when the fluctuating density peaks actually occur during the downwind progress and decay of any particular puff, a particular AEGL symptom onset will occur at vastly different times. Though we have a good method to integrate the toxic load for almost any time-dependent agent density trace, it is apparent from Figs. 5 and 6 that trying to approximate the ensemble of traces shown would be a fool's errand even having a good integration method in hand. A different approach is needed if the statistical variation of symptom onset times is to be reliably approximated. This difficulty is illustrated more concretely in the following section.

IV. Toxic Load Integrals for Multiple Agent Puff Realizations

The NRL Memorandum Report MR/6040–14–2014 (Boris and Patnaik, 2014), mentioned earlier, provides a fast, accurate software package called EAGLE to compute the toxic load integral as a function of time for any location, fixed or moving, where the agent density time history ("trace") is known. Figures 5 and 6 show the agent density time histories, for a measurement location at the center of the upwind X near Source 3 and at the center of the X about 4 km downwind of

Source 3 for all 16 independent realizations of the release. EAGLE was used to integrate the toxic load out to 100 minutes after release for the 16 traces in Fig. 5 and for the 16 traces in Fig. 6. In addition, the toxic load integrals were integrated for the remaining four locations at the corners of each X, separated from the center by +/- 25 meters in x and y, bringing the number of integrals at each lavender X to 80 for Source 3. The toxic loads for the five upwind measurement stations closest to S3 are reported in the left 5 columns of Table 1 and the five downwind stations are reported in the 5 columns on the right.

	Cells only ~570 m downwind of Source 3					Cells ~4 km downwind of Source 3				
rlz #	385, 265	385, 275	390, 270	395, 265	395, 275	1085, 85	1085, 95	1090, 90	1095, 85	1095, 95
1	0.074	0.164	0.052	0.104	0.039	0.817	0.593	0.264	0.240	0.207
2	0.554	0.289	0.207	0.163	0.091	0.055	0.048	0.030	0.015	0.008
3	3.255	0.151	0.117	0.086	0.027	0.081	0.049	0.042	0.046	0.054
4	3.255	0.321	2.164	0.166	0.036	0.591	0.377	0.365	0.327	0.334
5	0.526	0.435	0.174	0.107	0.147	2.254	1.938	1.745	1.749	1.501
6	1.148	0.516	0.104	0.087	0.036	0.023	0.016	0.015	0.016	0.009
7	1.157	0.269	0.537	0.096	0.195	0.072	0.040	0.030	0.020	0.009
8	1.677	0.626	0.970	1.127	1.066	0.342	0.289	0.224	0.214	0.179
9	4.439	0.350	0.766	0.760	0.006	0.378	0.139	0.044	0.044	0.029
10	1.923	0.943	0.872	1.161	0.348	0.119	0.106	0.091	0.067	0.027
11	1.405	1.016	0.931	1.043	1.148	0.020	0.017	0.014	0.009	0.007
12	1.156	0.791	0.355	0.270	0.228	0.196	0.145	0.135	0.136	0.107
13	3.403	1.036	1.118	0.935	0.146	0.195	0.171	0.147	0.129	0.148
14	1.596	5.310	5.186	7.601	2.604	6.116	6.798	9.035	11.16	9.436
15	1.454	1.292	1.202	1.300	0.359	3.895	3.728	3.320	3.502	3.742
16	1.262	1.252	1.245	0.671	0.743	0.874	0.494	0.499	0.438	0.239
avg	1.622	0.923	1.000	0.980	0.451	1.002	0.934	1.000	1.132	1.002

Table 1: Normalized toxic load integrals for 16 independent realizations of an acute release at Source 3 measured at 5 nearby stations near the source (left columns) and far from the source (right columns). Variations over a factor of 1500 are obtained.

The column headings in Table 1 give the I and j indices of the measurement station in the 1200 by 800 CFD grid. The toxic loads are strongly correlated for each realization (i.e. similar numbers in each horizontal row of 5) because the five stations are all relatively close together. Green highlights the realization with the smallest toxic loads, both at the upwind and at the downwind lavender X. Blue indicates the realizations with the largest toxic loads. Note that the smallest toxic loads occur for different realizations at the 5 stations near S3 and for the 5 stations far from S3. On the left nearer the source, the toxic loads vary by about a factor of 200 from the smallest to the largest and the values seem to have a rather uniform distribution. On the right farther from the source, the toxic loads vary over a range of about 1500, again rather uniformly distributed. For realization 14, the blue-highlighted toxic load integrals vary by more than a factor of four over distances of less than 75 meters more than half a kilometer downwind of Source 3. These results, though limited, strongly suggest that an approach that attempts to approximate an ensemble agent time-history trace, no matter how accurately, and then integrates that approximate time history will significantly under estimate the actual threat.

V. Ensemble Limiting Solutions Point to Plausible Worst Cases

The results of Table 1 strongly suggest that many more scenarios must be considered with a range of source strengths to determine the conditions where adverse symptoms are a plausible threat. To obtain a conservative prediction in which symptom onset does not occur for areas predicted to be safe, we are forced to consider low-probability realizations of the scenario that can occur given the overall environmental and wind parameters but usually do not. The puff/plume data base (Boris and Obenschain, 2018) provides detailed data for this extended study. Figure 7 below plots a distribution of symptom onset delays past the time when the agent can first arrive at a location. The figure is based on many separate toxic load integrations of the symptom onset delay using an ideal quadratic power law as the toxic loading rate. This quadratic law spans all density values and is not identical to chlorine, which has a limited range of quadratic dependence bounded by a low-density threshold.

Fig. 7 shows the distribution of onset delays for Source 3 measured at the upwind 1 km^2 (top panel) and the downwind 1 km^2 (bottom panel). The areas considered are the two square kilometer measurement areas for Source 3 that are shown in Fig. 4. There are 40,000 CFD cells in each of these regions (200 x 200 @ 5m^2). For these cells, the density time series for each of the 16 distinct realizations has been integrated using quadratic toxic loading until the onset toxic load of 1.0 is reached. The toxicity is set so that an agent density of 1 mg/m^3 held constant trips the toxic load onset condition in 20 minutes. Quadratic loading, therefore, means that an agent density of 5 mg/m^3 trips the onset condition in less than a minute. Stopping the integration at a toxic load of 1.0 yields the actual symptom onset time for each scenario considered. This time varies from scenario to scenario because the density as a function of time varies and because each scenario has a different time of agent first arrival. The onset delay time is the actual symptom onset time minus the agent earliest (first) arrival time, found by recording when the agent density first exceeds a small percentage of the maximum value.

For each scenario in the entire ensemble, the symptom onset delay time in minutes is plotted on the vertical axis in Fig. 7 versus the maximum agent density encountered at any time during the scenario. The maximum density is plotted with a logarithmic horizontal scale in density units of mg/m^3. Ten different values of the source strength are used, implemented by multiplying the recorded density traces by 0.01, 0.02, 0.05, 0.1, 0.2, 0.5, 1.0, 2.0, 5.0, and 10.0. These are indicated by ten different colors in the figure; lavender points used a 0.01 multiplier and red points used a multiplier of 10.0. Source strength is a free parameter here because the toxic loading is assumed to be quadratic everywhere. This source-strength rescaling gives enough independent toxic load integrals to get nearly continuous distributions. Many of the 6.4 million possible integrals for each source concern cells inside of buildings and these are discarded. For the remaining, many of them have agent densities that are too small to reach the health effect (symptom) onset time within one hour of the agent first arrival time at the cell in question and these also are not plotted. About 3 million scenarios remain for each source in Fig. 7.

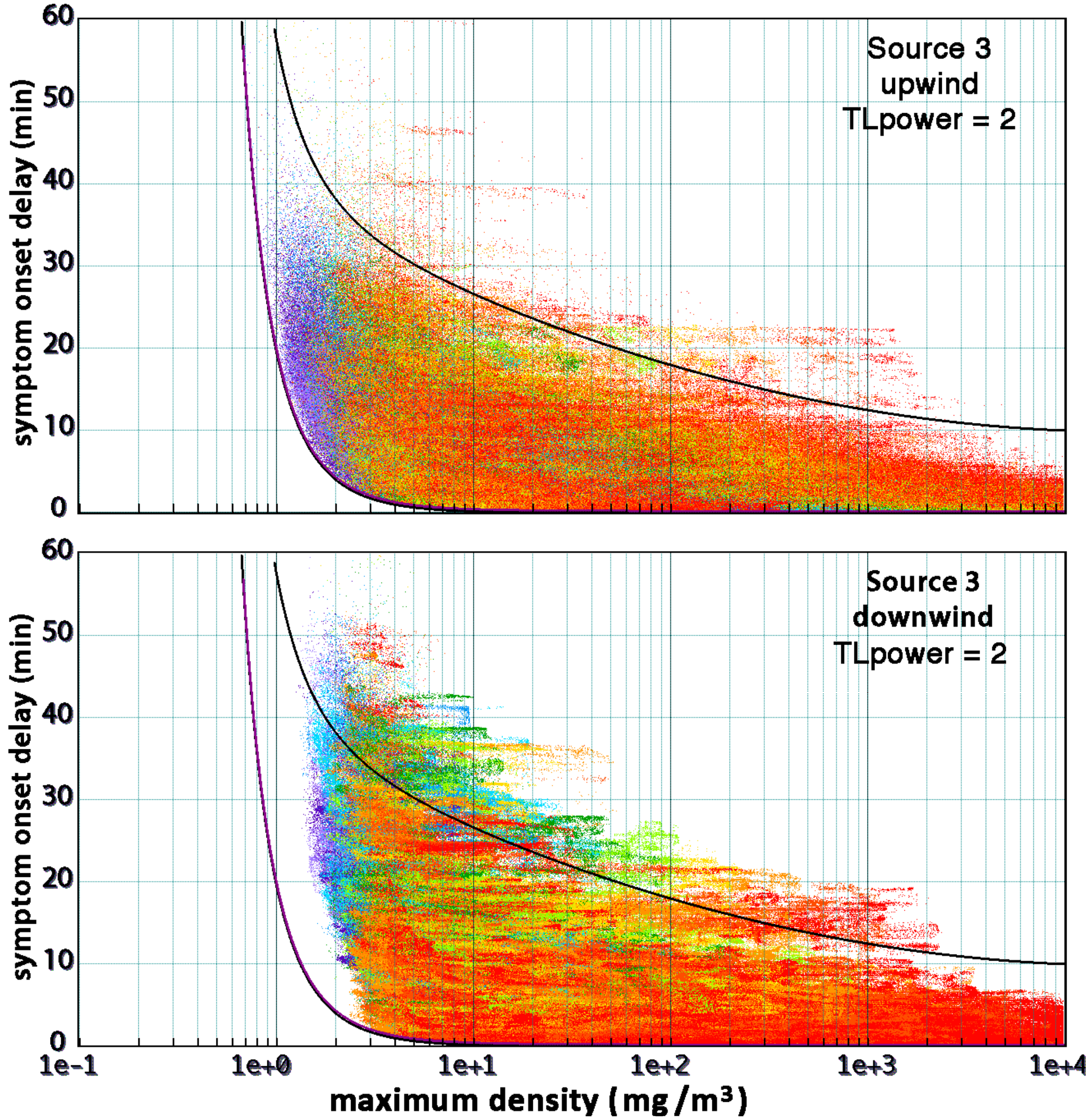

Figure 7. Symptom onset delay after 1st arrival vs maximum density. Quadratic nonlinearity TLpower = 2). Top panel: Source 3 over 1 km^2 about 0.5 km from S3. Bottom panel: Source 3 over 1 km^2 about 4 km downwind of S3.

The symptom onset delay time after first arrival is plotted vertically. The flat lower limit of the distributions occurs because the density is so high, once the agent actually arrives, that symptom onset, i.e. AEGL 1, 2 or 3, occurs in just a few seconds. When the maximum density for the trace is smaller, say 2 mg/m^3 for example, the onset delay time becomes appreciable. The lower black curve in each panel of the figure is the toxic symptom onset delay computed by EAGLE assuming that the agent density is constant in time after first arrival at the maximum density value. This is clearly a worst case since the maximum density does not necessarily arrive directly after the agent first arrives and the density will not necessarily stay constant after reaching its maximum value. Figure 7 shows that the worst cases for each source, which are adjacent to the lower black curve, occur often enough to be of concern. These are the scenarios that first responders and emergency managers need for decision making: when they can expect symptom onset for at least some members of an exposed population.

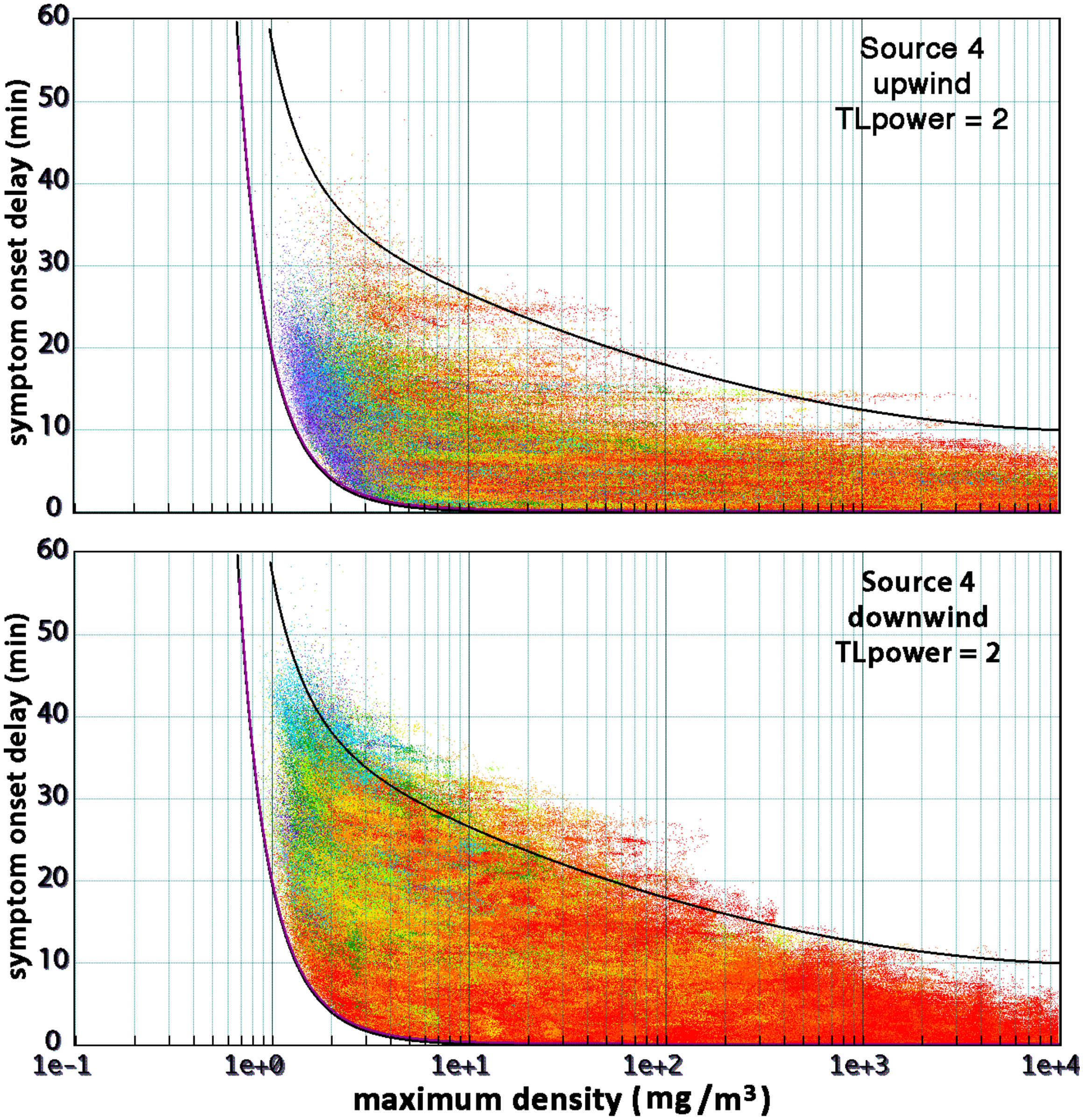

Figure 8. Symptom onset delay after 1st arrival vs maximum density. Quadratic nonlinearity. Top panel: Source 4 over 1 km^2 about 0.5 km from S4. Bottom panel: Source 4 over 1 km^2 about 4 km downwind of S4.

Figure 8 just above shows the same two distributions as computed for Fig. 7 but using the two square kilometer areas in the path of agent from Source 4. Figure 8 shows that the ensemble lower bound, marked by the lower black curve, is a somewhat closer fit to the distribution for Source 4 than for Source 3, at least for the lower panel of Fig. 7. The depletion zone for Source 4 adjacent to the bounding curves is smaller. This difference can be attributed to the different placement of these two sources. S3 is in the immediate recirculation zone of a building and thus the maximum density anywhere is a lot smaller for Source 3 than Source 4, as can be seen in Fig. 4. Furthermore, the downwind release of Source 3 agent is more drawn out than for Source 4.

These two effects mean that few of the scenarios, which fall in the Source 3 depletion zone with maximum densities of 1 to 3 mg/m^3, persist for long enough to accumulate a toxic load of 1.0. The limiting black curve for Source 4 is a good approximation to the distribution all the way down to 1 mg/m^3 maximum density. A modification to the formula, perhaps involving the total dose at each location to indicate whether there is enough agent passing each location to accumulate a toxic load of 1.0, should be developed to account for these depletion zones. This is left for future work.

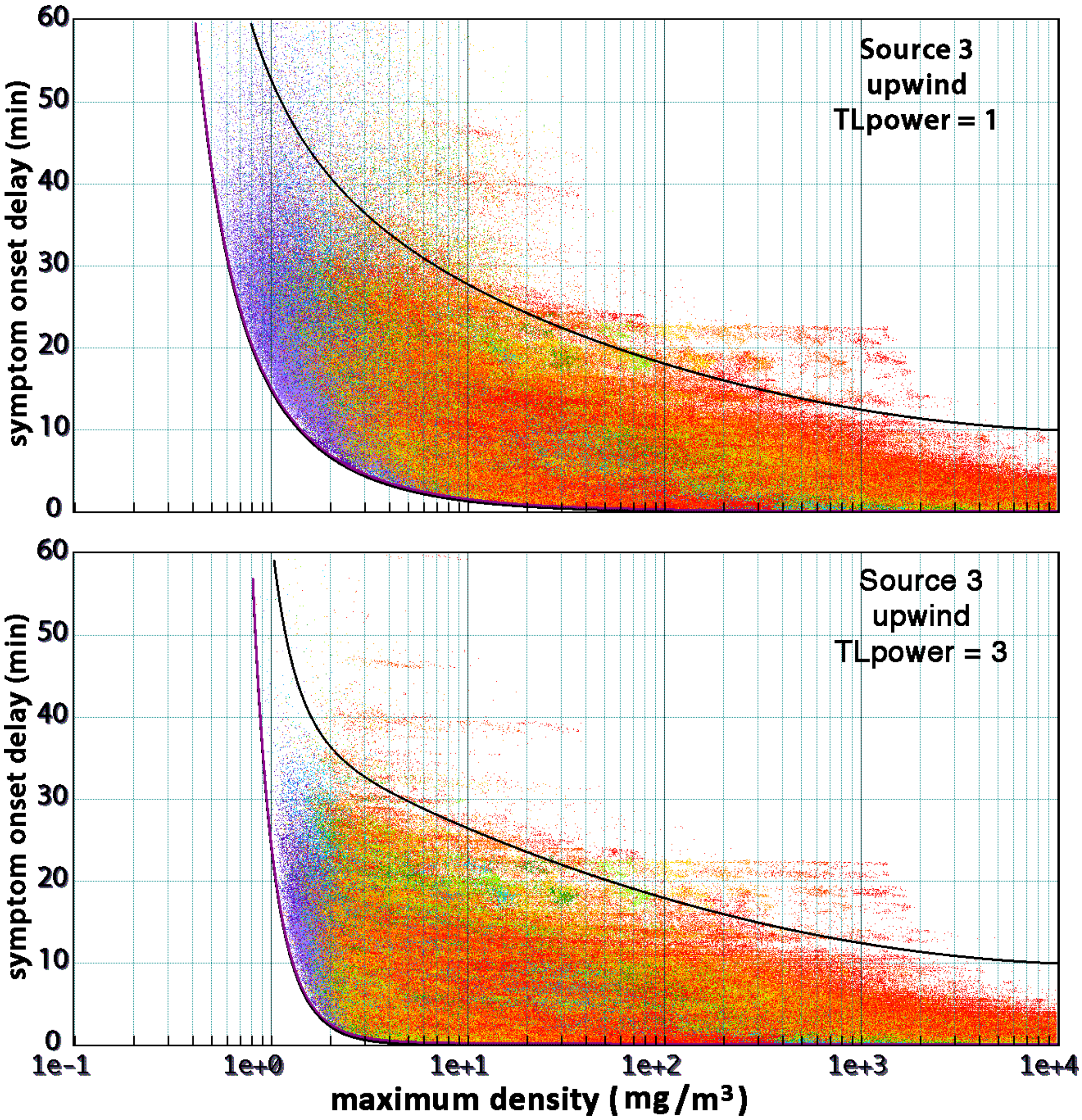

Figure 9. Symptom onset delay after 1st arrival vs maximum density. Top panel: Source 3 Toxic Load power = 1 (dosage) over 1 km^2 about 0.5 km from S3. Bottom panel: Source 3 Toxic Load power = 3 (cubic nonlinearity) @ over 1 km^2 about 0.5 km from S3.

Figure 9 above presents the toxic load distributions for the upwind 1 km^2 measurement area adjacent to S3 using toxic load power law exponents of 1 (linear dosage – top panel) and 3 (cubic nonlinearity – bottom panel). These results show differences from the quadratic nonlinearity used in the top panel of Fig. 7 but these differences are in the directions expected. The linear power-law ensemble limit is a shallower curve and the cubic power-law ensemble limit is a steeper curve than the quadratic nonlinearity of Figs. 7 and 8. In Fig. 9, the distributions are again adjacent to the limiting curve throughout almost the entire maximum density range.

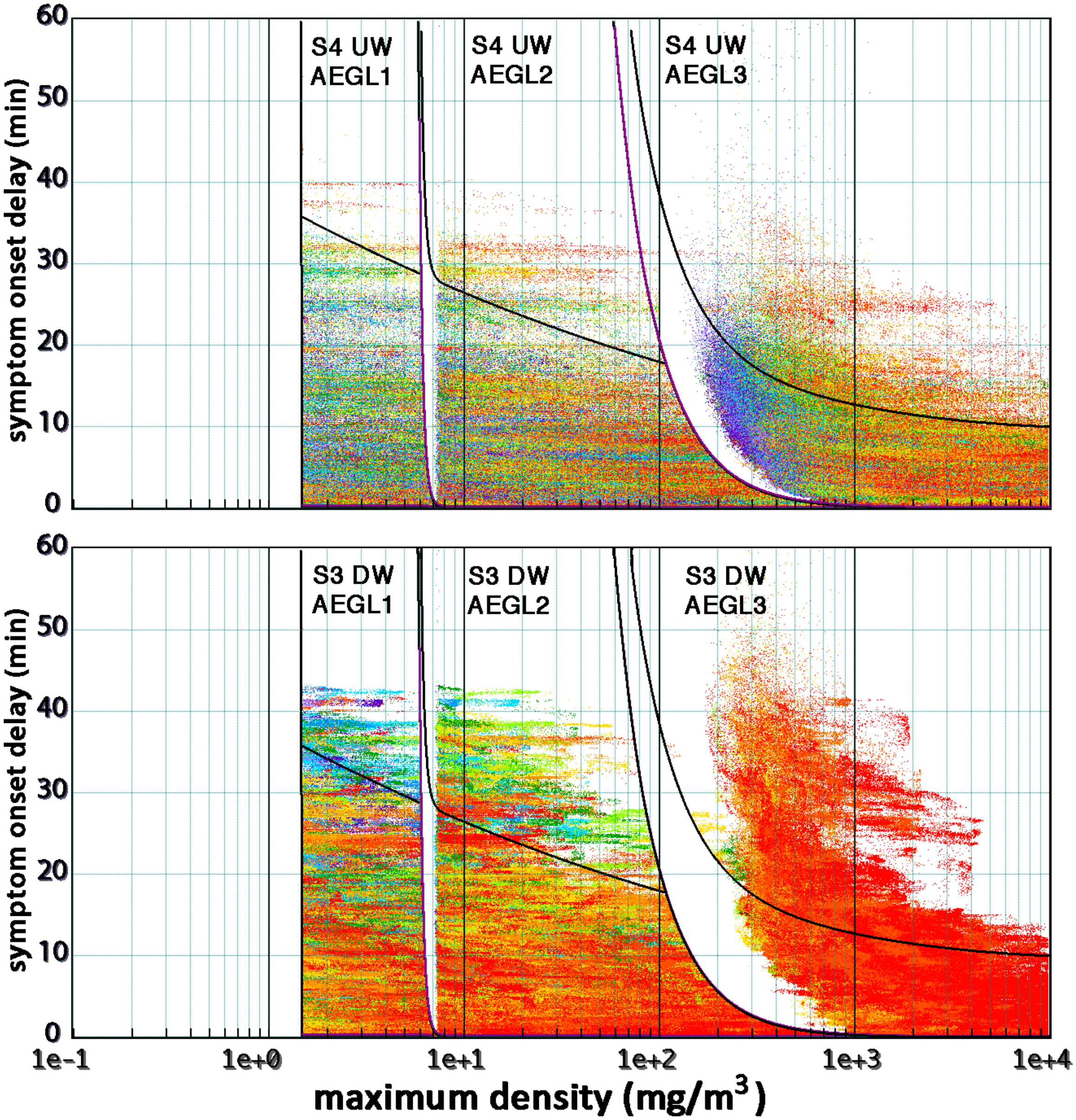

Figure 10. Chlorine symptom onset delay after 1st arrival vs maximum density. EPA AEGL 1, 2, & 3 superimposed. Chlorine has onset thresholds and a near quadratic nonlinearity. Top panel: Source 4 over 1 km^2 about 0.5 km from S4. Bottom panel: Source 3 over 1 km^2 about 4 km downwind of S3.

Figure 10 immediately above repeats the toxic-load distributions shown in Figs. 7 and 8 but now using the EPA data for chlorine AEGLs as interpolated and generalized in the EAGLE package. The three Acute Exposure Guideline Levels (AEGLs) are superimposed in a single plot for the Source 4 upwind scenarios (top panel of Fig. 10) and the Source 3 downwind scenarios (bottom panel). The full complexity of the chlorine toxic loading behavior is on display in this figure. AEGL

1 has an immediate symptom (i.e. watering eyes) onset density of 1.47 mg/m^3 with no regard for the duration of exposure. This is perfectly captured in the AEGL 1 distributions shown on the left in each panel. AEGL 2 has a steep quadratic nonlinearity for maximum densities below about 6 mg/m3 and a rapid symptom onset (deleterious, possibly permanent effects) for higher densities. AEGL 3 on the right of each panel, for possibly fatal exposures, has an approximately quadratic nonlinear behavior throughout the density range.

Notice that the depletion zone for chlorine's AEGL 3 is quite severe. The length of time taken to accumulate a fatal exposure, even with chlorine densities as high as one part in a thousand, is sufficiently long that the agent puff dissipates before a toxic load can be accumulated. In the close-packed buildings of the upwind 1 km^2 measurement area of Source 4, the contaminating agent is retained somewhat longer allowing a smaller depletion zone. However, it is still significant. What the reader should take away from these last tests is that taking the maximum density and assuming the density is constant until the full toxic load is accumulated is a good approximation to the few but plausible scenarios that pose the worst threats. Further, this simple formulation is equally applicable for real agents as for the ideal power law formula used in Figs. 7 and 8.

VI. Plausibility and Practicality of these Worst-Case Predictions

At first glance, it seems highly unlikely that two numbers, the maximum possible density and the earliest time the agent first arrives at the location of interest taken over the entire ensemble of realizations, should determine the worst-case symptom onset time for all three AEGL health effects (symptoms) for all agents, source strengths, and source locations. Remember, however, we are seeking only an attainable worst case to ensure that the health effect predictions for exposure are on the conservative "safe side." Furthermore, this simple formula for the ensemble limiting onset delay time, captured by the lower black lines in Figs. 7, 8, 9, and 10, has a dense set of scenarios adjacent to the limit to make these worst cases plausible.

The onset of any symptom cannot occur before the agent can first arrive at the location of interest. Further, the maximum agent density ever observed at that location determines the fastest toxic-loading rate possible. The shortest possible time for the toxic load to accumulate to 1.0 will occur if the agent density stays at the maximum value for at least the inverse of the toxic-loading rate for that agent. it will not always be the case that the maximum density in the agent time history at a location occurs at the earliest time of agent arrival or that it persists at the maximum value for long enough. These two quantities, however, are at least correlated. If agent arrival is delayed, the density is usually smaller because much of the agent has gone somewhere else first. Figure 5, presenting agent time histories at a location of interest relatively close to the source, shows that the maximum density for all 16 realizations occurs shortly after agent first arrival, which happens at 5 to 6 minutes after release for Source 3. Figure 6, presenting agent time histories at a location much farther from Sourced 3, shows that the maximum density for each realization's trace is delayed somewhat more than in Fig. 5. However, this delay is about the same as for Fig. 5 relative to the agent first arrival times.

Figure 7 shows that the distribution of symptom onset delays is dense just above the lower black line. This line is the ensemble lower limit, not just a possible worst case. The probability of symptom onset is high enough adjacent to this lower limit that it should be considered as not just a statistically possible threat but a plausible actual threat, the condition emergency managers will relate to directly. If this new health-effects diagnostic can be implemented in CT-Analyst®, it would give an area-wide display of the time after agent release when a particular symptom (AEGL 1, 2 or 3) could first manifest at each location. These symptom onset times would appear as nested contours near the source and contours extending off the urban computational domain when the particular symptom can no longer appear because the agent density is too low or the exposure duration is too short. Each AEGL condition would have to be presented as a distinct display because there is so much information to plot for each AEGL.

Assuming that the ensemble minimum symptom onset time is a plausible solution to the problem of computing meaningful health effects, the obvious question is whether it is practical to compute. Can this approach be implement in a real-time system like CT-Analyst in a fast, accurate manner? Figures 11, 12 and 13 below are presented to answer this question provisionally by presenting some preliminary results. Figure 1 showed the location of Source 4 (S4). Source 4 agent enters a complex urban geometry and this provides a stringent test. Figure 11 plots the time of earliest agent arrival at each location in the domain. This is the minimum of all 16 separate realization arrival times. During the 100 minutes of the puff simulations, none of the 16 realizations of the Source 4 release has reached cells colored gray in this figure.

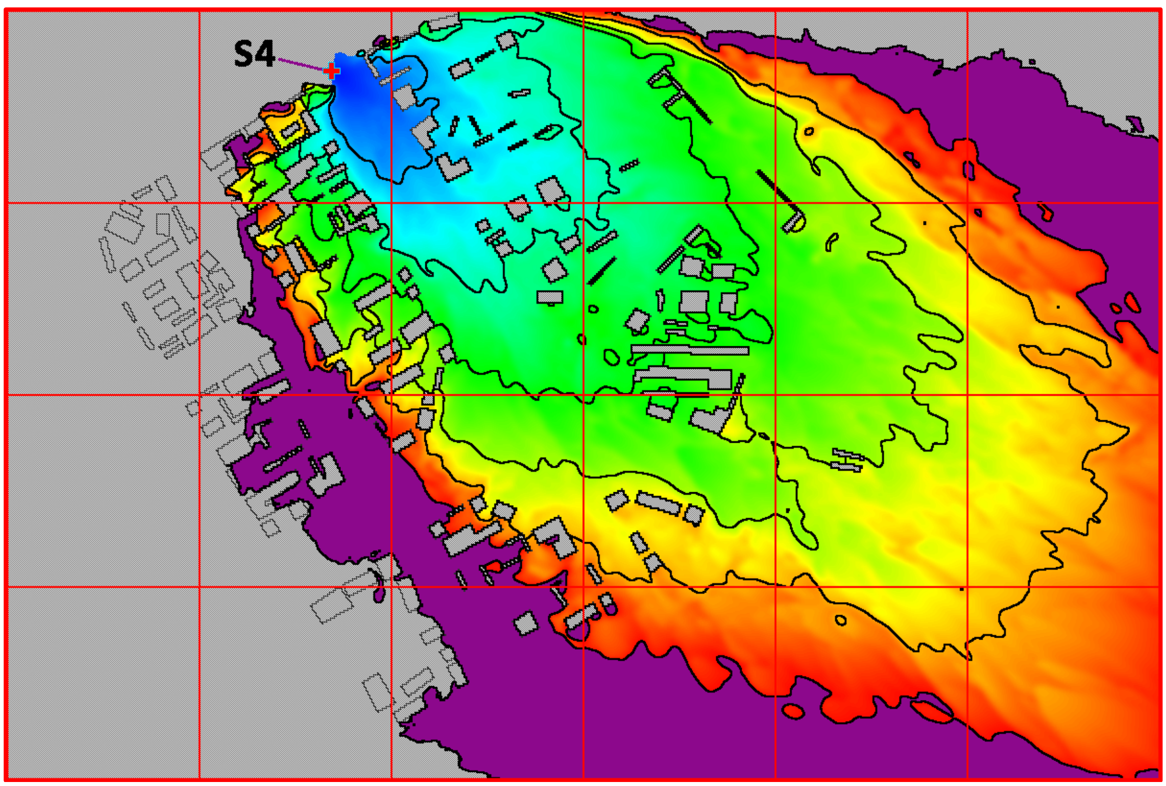

Figure 11: The time of first agent arrival at each point, over the entire ensemble of 16 releases from Source 4 in Fig. 1. This is a relatively smooth function and has no time dependence. Symptom onset must always occur sometime later than the time of first agent arrival. Five minute intervals are indicated out to 30 minutes.

The red cross identifies the location of Source 4 in Figs. 11, 12 and 13. Figure 11 shows that the earliest arrival time is generally a monotonically increasing function away from the source.

However, one can imagine situations, based on building geometries where this will not be the case locally. For example, an upwind building may kick the agent upward so it arrives from above in a courtyard or in some area sheltered by buildings before it arrives in the street upwind of the building. The blue area in Fig. 11 around Source 4, indicates an earliest (first) arrival time less than 5 minutes. Each successive black contour marks another five minutes. It is easy to see that these black contours, although ragged, are nicely nested and could be well approximated by smooth contours. It is also possible that these constant arrival-time contours may actually become smoother as more realizations of the ensemble are considered.

Figure 12 shows the maximum density found in the ensemble of realizations originating at Source 4. The maximum for the 16 realizations was taken over time out to 100 minutes at each location in the domain. For most contaminated locations 100 minutes is long enough but, near the edges of the cloud in Fig. 12 where the blue color indicates a very low maximum density, there is the possibility that a later time or additional realizations make expand the cloud in Fig. 12 somewhat. In such cases, however, the cloud in Fig. 11 would expand somewhat as well.

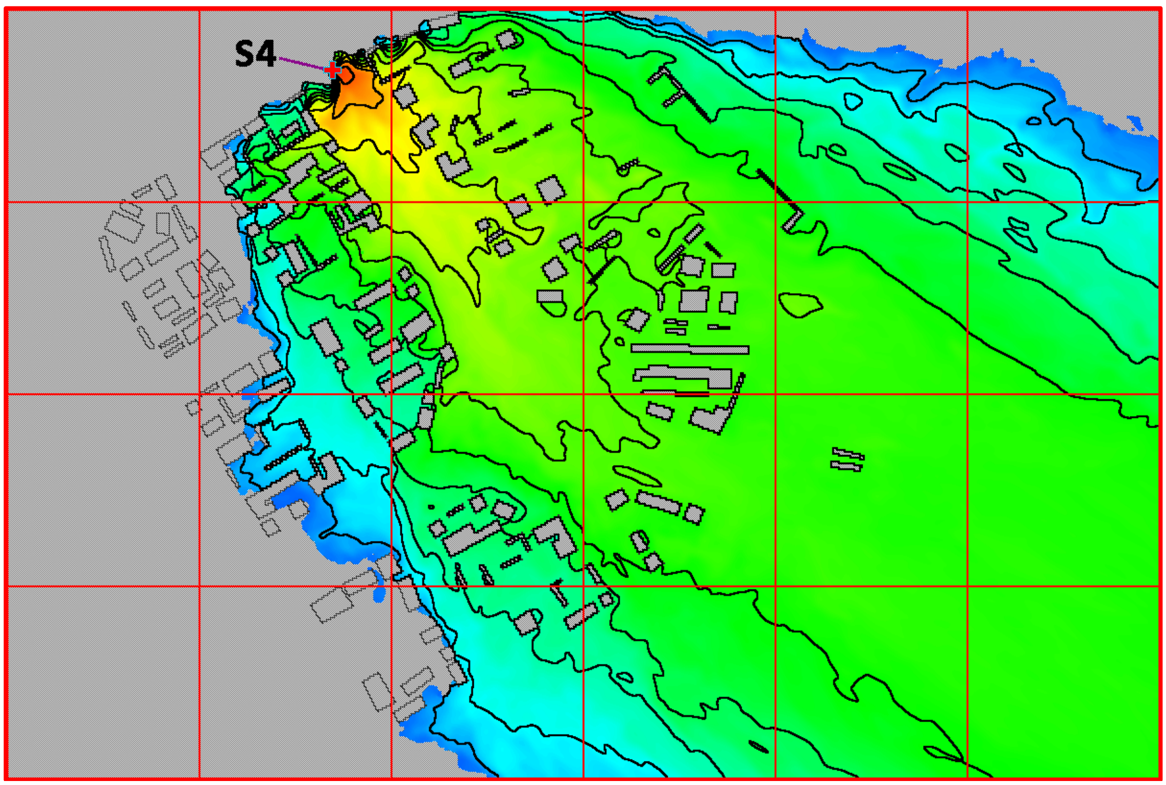

Figure 12: A single maximum density field can be calculated for the ensemble of 16 releases at S4 in Fig. 1. This function is relatively smooth with no time dependence, lending itself to approximation in real-time models. Factor of 10 density contour levels are indicated in black.

Although the structure of the ensemble maximum density differs appreciably from the ensemble earliest arrival time in Fig. 11, we can also imagine approximating this function satisfactorily with smooth contours as well. The black contours here indicate successive order-of-magnitude reductions in the agent maximum density. The edge of the puff, at very low density, here indicated by blue, can be quite ragged with a number of geometry-determined wisps and edges. In constructing a smoothed representation as input for the symptom onset time computation, there should be a first (earliest) arrival time for every non-zero maximum density and a maximum density for every finite first arrival time. In addition, the modeled ensemble first arrival time should everywhere by no later than any known arrival time and the modeled ensemble maximum density should everywhere be no smaller than any known maximum density when there is trusted data.

Figures 11 and 12 are the input data needed to calculate the symptom onset times for contamination from S4 using the ensemble limit formula discussed and justified above. Using the maximum density from Fig. 12, yields a symptom onset delay time past first agent arrival based on the same quadratic toxic-loading law used to generate Figs. 7, 8 and 9 above. We also have the first (earliest) arrival time of the agent from the data in Fig. 11. Adding these two times together gives the symptom onset time shown in Fig. 13 just below. This is the summary prediction that crisis managers and first responders will likely find most useful – though it does require an estimate of the source agent and its amount to evaluate the toxic loading rates.

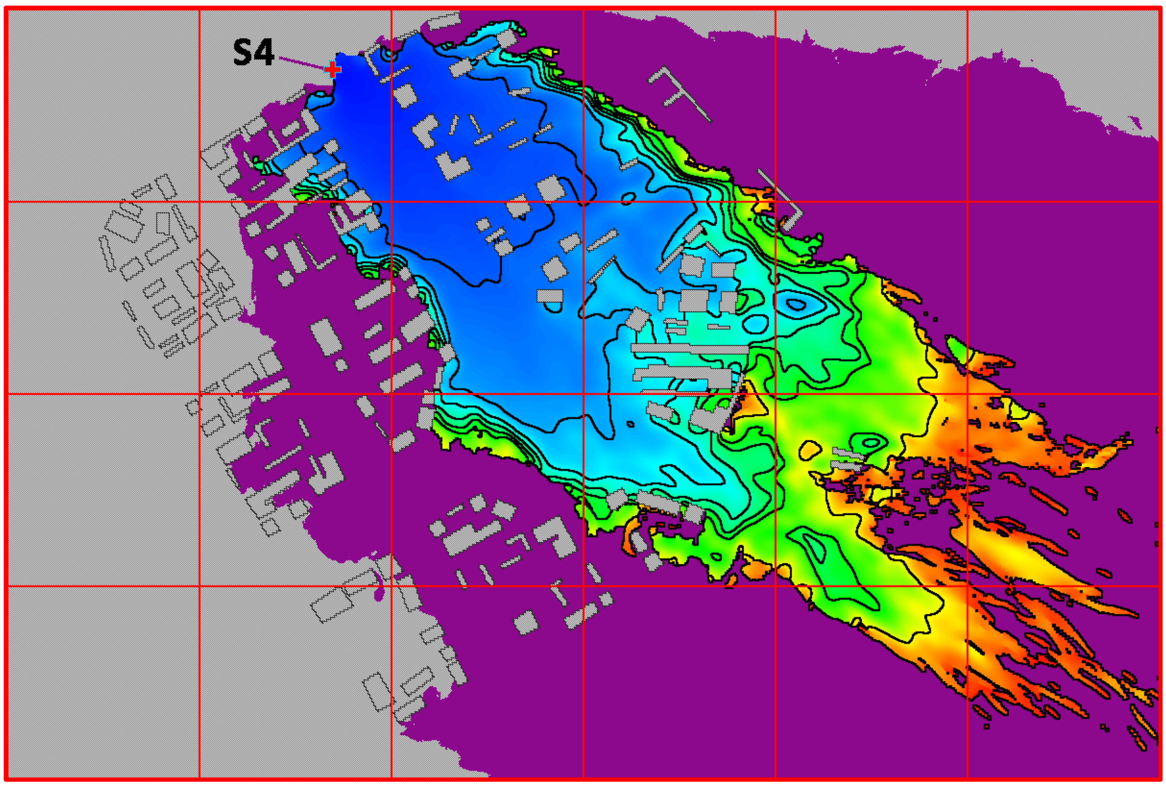

Figure 13: The ensemble symptom onset time for a quadratically toxic agent released at S4 in Fig. 1. This function is also relatively smooth for short times but becomes increasingly complex as late time symptom onset is approximated.

In Fig. 13, the symptom onset times out to one hour in 10-minute intervals are indicated by the black contours. The two outer contours, in the yellow and red, mark the 90 minute and 2 hour symptom onset times. Magenta covers locations in the urban domain where a low density of the agent has reached in at least one of the 16 realizations of Source 4 during the 100-minute simulation but where the generic symptom effect being evaluated does not onset within two hours because the maximum density achieved at that location is not high enough. Figure 14, just below, shows the minimum (earliest) symptom onset time evaluated when using only the 16 realizations computed for Source 4 without applying the ensemble limit formula based on Figs. 11 and 12. First arrival always occurs further from the source than the symptom onset time.

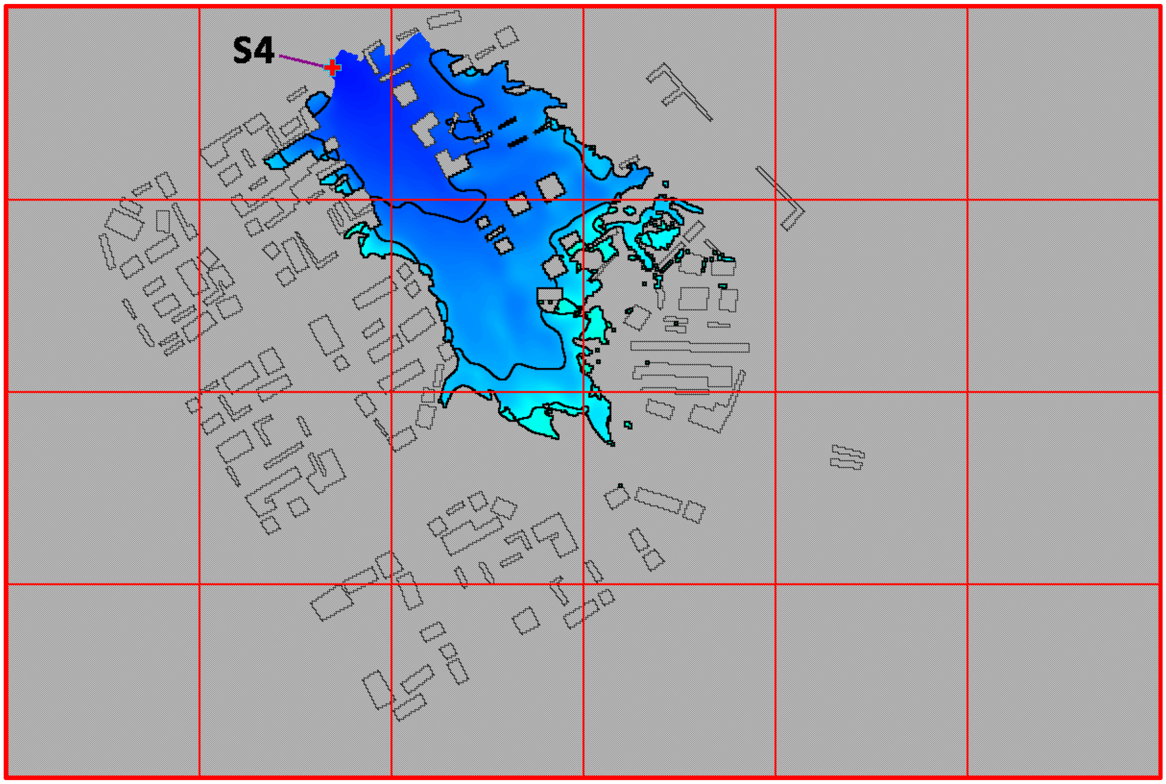

Figure 14: The minimum symptom onset time for a quadratically toxic agent released at S4 found in at least one of the 16 realizations. 1. These symptom onset times are longer than the corresponding symptom onset times computer using the ensemble limit formula.

Figure 13 approximates the entire symptom onset time evolution of the ensemble toxicity. This plot is not time dependent. Comparing the inner 10-minute contour in Fig. 13 to the second (10-minute) contour in Fig. 11, we see that these two contours are recognizably the same although first arrival of the agent does occur a little earlier than symptom onset – as it should. Comparing the 20-minute contours, however, shows that there is now a significant symptom onset delay between the first agent arrival and the actual symptom onset. This occurs because the maximum agent density, this far from the source, has already dropped enough that the time to accumulate a full toxic load because comparable the agent arrival time. The area inside the agent first-arrival contour at a given time is always more inclusive than the symptom onset area because of this onset delay. In early times the symptom onset time contours are well organized and nested. However, by 30 minutes and later, the contours become increasingly varied and jumbled. Small pockets of earlier symptom onset, caused by local upwind building influences, are observed in the 90-minute and 2-hour areas.

Figure 14 above presents the earliest actual onset time computed at each location from the 16 FAST3D-CT realizations of the instantaneous release at S4. Each separate realization was integrated using the EAGLE formula for the quadratic toxicity law and the actual symptom onset was recorded. The 10, 20, 30, and 40 minute onset times are contoured in Fig. 14, as for Fig. 13, and the same continuous color scale is used for these symptom onset times. In Fig. 14 the symptom onset time is computed using only the minimums of the 16 realizations we have without application of the ensemble limit formula. Notice that the areas inside these contours are smaller, i.e. less conservative than in Fig. 13. Figure 14 projects later symptom onsets than Fig. 13 at each location because it is not based on the estimates of the entire ensemble as a whole. In both figures, the inner contour around the dark blue area represents the region where symptom onset can be expected within 10 minutes for at least some of the exposed population with a high enough probability to be of concern. Figure 13 is a conservative prediction that includes consideration of low probability scenarios where the symptom onset occurs at the earliest possible times. Exactly how conservative this prediction is not certain, however, Figs. 13 and 14 show that the 10-minute threat area increases by less than a factor of 2 using the conservative formula underpinning Fig. 13. Figures 7 through 10, as remarked earlier, indicate that the distribution of symptom onset times is dense near the ensemble lower limit implemented in Fig. 13.

Symptom onset times beyond about 30 or 40 minutes in Fig. 14 are not found, though some additional contours appear in Fig. 13, because the particular set of 16 realizations we have can not show symptom onset for later times as the onset delay becomes longer than the duration of the run. Symptom onset does not have to occur everywhere even if we wait forever, and certainly not within a limited domain.

VII. Conclusions and Future Work:

A simple, fast alternative to integrating the toxic load for predicted or measured agent density time histories, which is guaranteed to be conservative, has been presented and justified for instantaneous "puff" releases. This alternative method requires evaluating the toxic loading rate for the maximum possible density at each location, taken over the full ensemble of possible realizations, and it will be much faster than performing the toxic load integral instead, which involves taking many timesteps. This approach takes into account the low-probability realizations that constitute the maximum threat and which are difficult to evaluate by experiment, field trial or simulation. In the bargain we obtain a function, for each AEGL, that applies for the entire scenario and is not a function of time. Rather it displays the entire time history of the chosen health effect at once. One conclusion of this paper has been to show how the complexity of the severe multi-realization variability of the possible toxic loads actually works for us in this case by simplifying the worst-case limits that determine the predictions needed for public safety.

The main way to implement this simplification is to develop models for the ensemble-integrated variables $\rho_{max}(\vec{x})$ and $t_{arrival}(\vec{x})$ so that the calculation can be included directly in operational real-time models. If the ensemble maximum dose can also be estimated, it sets a limit to the amount of agent available over time at each location in the domain. This information may be enough to approximate, at least roughly, the low-density depletion region identified in Fig. 7 where the symptom onset delay can approach infinity if there is not enough agent to maintain the maximum density for long enough. The corresponding onset-time simplifications for continuous-source plumes is not considered here but is a worthy research goal for the future. In a continuous plume, the toxic load will continue to accumulate with time everywhere there is sufficient contamination. Thus symptom onset will eventually occur, at least at some AEGL level, as long as the necessary thresholds are reached.

Future research can also tell us how much larger the maximum density in a much larger ensemble can be at each location. This ratio will almost surely depend on time as well as location. Wind tunnel testing, which has advanced continuously of the last two decades (e.g. Harms, et al., 2011; Leitl, et al., 2013, 2015), allows many more realizations than detailed simulation. It should be used to determine statistically more accurate values of the ensemble earliest agent arrival time and the ensemble maximum density and how the results of these larger ensembles can be approximated by the limited ensembles available to detailed simulation. Part of this research task is to find an approximate reduced-order model for the ensemble earliest agent arrival time as a function of location suitable for use by models like CT-Analyst. We also seek a density profile that can be computed by CT-Analyst to conservatively approximate the expected maximum density at each location. One possible approach is to scale the underlying CT-Analyst density prediction to account for the full spectrum of possible fluctuations. This scale factor will have to be a function of the agent and its toxic loading-rate dependence.

Looking toward the future, the computations and limited parameter survey reported here should be extended. All six sources available in the puff database can be analyzed and the number of realizations can, in principle, be increased. The nonlinear toxic loading exponent, treated as 2.0 (quadratic) here, must be varied and real agent toxic loading formulae can be used as with chlorine above. Finally, the reduced order models for the maximum density and the arrival time, should be tested by simulation and wind tunnel campaigns for a different complex urban geometry.

Acknowledgements

Special thanks are due our colleagues Adam Moses, Keith Obenschain and Mi-Young Obenschain for their numerous contributions to the technology we have used over the last five years in herding this effort forward. The research leading to this capability and preliminary demonstration was supported by the project on “Highly Complex Fluid Dynamics” within the ONR/NRL 6.1 basic research core program.

References

Boris, J.P., G. Patnaik, M-Y. Lee, T. Young, B. Leitl, F. Harms and M. Schatzmann (2009), Validation of an LES Urban Aerodynamics Model for Homeland Security, 47th AIAA Aerospace Sciences Meeting, AIAA Paper 2009–1633, Orlando FL, 5–8 January 2009, (AIAA, Reston VA, 2009).

Boris, J.P., Patnaik, G., Obenschain, K., Delaney, J., and Donnelly, J. (2010), “Fast and Accurate Prediction of Windborne Contaminant Plumes for Civil Defense in Cities,” Proceedings: Computational Wind Engineering Conference 2010 (CWE'2010), Chapel Hill NC, 23–27 May 2010.

Boris, J.P. and Patnaik, G. (2014), “Acute Exposure Guideline Levels (AEGLs) for Time Varying Toxic Plumes,” NRL MR/6040–14–2014.

Boris, J.P. and Obenschain, M-Y. (2018), “Airborne Puff and Plume Datasets for an Urban Landscape,” NRL Memorandum Report (53 pages – in preparation).

Harms, F., Hertwig, D., Leitl, B., Schatzmann, M., Patnaik, G. (2011), “Characterization Of Transient Dispersion Processes In An Urban Environment,” Proceedings: 14th International Conference on Harmonization within Atmospheric Dispersion Modeling for Regulatory

Purposes, Kos Island, Greece, 2–6 October 2011.

Holt, T., Pullen, J., and Bishop, C. (2009), "Urban and ocean ensembles for improved meteorological and dispersion modeling of the coastal zone," *Tellus*, **61A**: 232–249, 2009.

Holt, T., Cummings, J., Bishop, C., Doyle, J., Hong, X., Chen, S., and Jin, Y. (2011), "Development and testing of a Coupled Ocean-Atmosphere Mesoscale Ensemble Prediction System (COAMPS-OS)," *Ocean Dynamics* **61**: 1937–1954, 2011.

Leitl, B., Hertwig, D., Harms, F., Schatzmann, M., Patnaik, G., Boris, J., Obenschain, K., Fischer, S., and Rechenbach, P. (2013), "Large Eddy Simulation of Accidental Releases," in **Progress in Turbulence V**, Springer Proceedings in Physics **149**, A. Talamelli, M. Oberlack and J. Peinke (Eds.), 2013.

Leitl, B., Harms, F., Berbekar, E., Patnaik, G., Boris, J., Schatzmann, M. (2015), "Wind Tunnel Experiments or Advanced CFD ... What Do We Need for Understanding Flow and Dispersion in The Lower Atmospheric Boundary Layer?" Proceedings: International Conference on Modeling Fluid Flows CMFF'15, Budapest, Hungary, 1-4 September 2015.

Oran, E.S and Boris, J.P. (2001), **Numerical Simulation of Reactive Flow: 5–5.1,** The Induction Parameter Model, pp 150–151, (2nd edition, Cambridge University Press, New York NY, 2001).

Patnaik, G. and Boris, J.P. (2005), "Fast and Accurate CBR Defense: Bringing HPC to the Warfighter and First Responder," AIAA Paper 2005–7166, 1st AIAA InfoTech@Aerospace Meeting, Arlington VA, 26–29 September 2005.

Patnaik, G, Grinstein, F.F., Boris, J.P. Young, T.R. Jr., and Parmhed, O. (2007), "Large Scale Urban Simulations," Chapter 17, pp 502–530, in **Implicit Large Eddy Simulation: Computing Turbulent Flows**, F. Grinstein, L. Margolin, and W. Rider (eds), Cambridge University Press, 2007.

Stage, Steven A. (2004), "Determination of Acute Exposure Guidelines in a Dispersion Model," *Journal of the Air and Waste Management* Association **54**: 49–59, ISSN 1047-3289, Jan 2004.

Sweeney, L.M., Sommerville, D.R., and Stephen R. Channel, S.R. (2014), "Impact of Non-constant Concentration Exposure on Lethality of Inhaled Hydrogen Cyanide," *Toxicological Sciences* **138(1)**, pp 205–216, doi:10.1093/toxsci/kft277, 2014.

Ten Berge, W.F., Zwart, A., and Appelman, L.M. (1986), "Concentration-Time Mortality Response Relationship of Irritant and Systematically Acting Vapours and Gases," *Journal of Hazardous Materials* **13**: 301–309, 1986.

U.S. Environmental Protection Agency AEGL Program (2018), https://www.epa.gov/aegl.